

An Adaptive Characteristic-wise Reconstruction WENO scheme for Gas Dynamic Euler Equations

Jun Peng^{a,b}, Yiqing Shen^{b,*}, Heng Yong^a, Chuanlei Zhai^a, Guoxi Ni^a

^a*Institute of Applied Physics and Computational Mathematics, Beijing 100094, China*

^b*State Key Laboratory of High Temperature Gas Dynamics, Institute of Mechanics,
Chinese Academy of Sciences, Beijing 100190, China*

Abstract

Due to its excellent shock-capturing capability and high resolution, the WENO scheme family has been widely used in varieties of compressive flow simulation. However, for problems containing strong shocks and contact discontinuities, such as the Lax shock tube problem, the WENO scheme still produces numerical oscillations. To avoid such numerical oscillations, the characteristic-wise construction method should be applied. Compared to component-wise reconstruction, characteristic-wise reconstruction leads to much more computational cost and thus is not suite for large scale simulation such as direct numeric simulation of turbulence. In this paper, an adaptive characteristic-wise reconstruction WENO scheme, i.e. the AdaWENO scheme, is proposed to improve the computational efficiency of the characteristic-wise reconstruction method. The new scheme performs characteristic-wise reconstruction near discontinuities while switching to component-wise reconstruction for smooth regions. Meanwhile, a new calculation strategy for the WENO smoothness indicators is implemented to reduce over-all computational cost. Several one dimensional and two dimensional numerical tests are performed to validate and evaluate the AdaWENO scheme. Numerical results show that AdaWENO maintains essentially non-oscillatory flow field near discontinuities as the characteristic-wise reconstruction method. Besides, compared to the component-wise reconstruction, AdaWENO is about

*Corresponding author

Email addresses: pengjun62@163.com (Jun Peng), yqshen@imech.ac.cn (Yiqing Shen), yong_heng@iapcm.ac.cn (Heng Yong), zhai_chuanlei@iapcm.ac.cn (Chuanlei Zhai), gxni@iapcm.ac.cn (Guoxi Ni)

20% faster which indicates its excellent efficiency.

Keywords: WENO scheme, characteristic-wise reconstruction, adaptive method, Euler equations

1. Introduction

Numerical simulation of compressible flow serves engineering and scientific researches by providing detailed and high-quality flow field information. For high-resolution and accurate simulation of compressible flow, numerical methods being applied shall be able to capture all important features, e.g. turbulence and shockwave, in the flow field.

The family of weighted essentially non-oscillatory (WENO) finite difference schemes [1, 2] has been widely used in compressible flow simulations due to its high resolution of small structures and good shock-capturing capability. Within the general framework of smoothness indicators and non-linear weights proposed by Jiang and Shu [2], many efforts have been made to improve the accuracy and efficiency of the WENO scheme. Henrick et al. [3] improved the accuracy of the WENO scheme at critical points by suggesting a mapping function. Borges et al. [4, 5] proposed the WENO-Z scheme which calculates the non-linear weights with a high order smoothness indicator. The WENO-Z scheme achieves lower dissipation and higher resolution than the classical WENO scheme of Jiang and Shu and has lower computational cost than the mapping function method of Henrick et al.. The accuracy of the WENO-Z scheme was further improved by Yamaleev and Carpenter [6, 7] and Fan et al. [8] by introducing higher order smoothness indicators. Fu et al. [9] proposed a family of high-order targeted ENO schemes which combines the idea of both the ENO scheme and the WENO scheme. Except for these improvements for the fifth order WENO scheme, higher order WENO schemes (higher than fifth order) were also developed [10, 11, 12].

To develop and improve a WENO scheme, two issues should be addressed at the same time: maintaining high order accuracy at smooth region and capturing discontinuity non-oscillatorily. Aforementioned methods mainly focus on the improvement of the accuracy of WENO schemes at smooth regions. Shen and Zha [13] showed that at transitional points, which connect smooth region and discontinuity, the accuracy of fifth order WENO schemes is second order and a multi-step weighting method [14, 15] was developed to improve the accuracy.

Inspite of their excellent performances for scalar problems, WENO schemes still produce numerical oscillations for problems like the Lax shock tube problem of the gas dynamic Euler equations. To get rid of such oscillations, the characteristic-wise reconstruction method [16, 2, 17] should be applied. Compared to the component-wise reconstruction method, the characteristic-wise reconstruction method results in much more computational cost. Therefore, for efficiency consideration, in practical large scale simulations, the component-wise reconstruction method is always preferred, e.g. [18], that some numerical oscillations are tolerable. However, such compromise may reduce the reliability of the simulation result that numerical oscillations disturb the flow field and may change the whole flow structure. To prevent numerical oscillations and avoid the use of characteristic-wise reconstruction, He et al. [19] analyzed the WENO weights and proposed a new method to calculate the final smoothness indicators. This method reduces but is not free of numerical oscillations. Puppo [20] proposed an adaptive method to combine the component-wise reconstruction method and the characteristic-wise reconstruction method and showed good performance and efficiency. Nevertheless, the flagging criterion in Puppo's method may misclassify smooth cells and thus reduces the computational efficiency of the scheme.

In this paper, we focus on developing an efficient and accurate characteristic-wise reconstruction WENO scheme which is of practical value for large scale simulation of compressible flow. A new adaptive characteristic-wise reconstruction WENO scheme utilizing a highly accurate switch function is proposed, and a new strategy for smoothness indicators calculation is also introduced to further reduce the computational cost of the WENO scheme. This paper is organized as following. In Section 2, the WENO scheme and its component-wise and characteristic-wise reconstruction implementations are introduced. In section 3, a new adaptive method is developed based on the analysis of the two implementations. In section 4, several numerical tests are presented to illustrate the performance and efficiency of the new method. Concluding remarks are given in Section 5.

2. Solving the gas dynamic Euler equations with WENO

2.1. The gas dynamic Euler equations

The one dimensional Euler equations of inviscid ideal gas is given by:

$$\frac{\partial \vec{U}}{\partial t} + \frac{\partial \vec{F}}{\partial x} = 0 \quad (1)$$

in which \vec{U} and \vec{F} are the conserved variable and the convective flux vectors:

$$\vec{U} = \begin{bmatrix} \rho \\ \rho u \\ E \end{bmatrix}, \vec{F} = \begin{bmatrix} \rho u \\ \rho u^2 + p \\ u(E + p) \end{bmatrix}, \quad (2)$$

where ρ is the density, u is the velocity, and $E = \frac{p}{\gamma-1} + \frac{1}{2}\rho u^2$ is the total energy with $\gamma = 1.4$.

For the convective flux vector \vec{F} , its Jacobian matrix \mathbf{A} is defined as:

$$\frac{\partial \vec{F}(\vec{U})}{\partial x} = \mathbf{A} \frac{\partial \vec{U}}{\partial x}, \quad (3)$$

where \mathbf{A} is written as:

$$\mathbf{A} = \mathbf{R}\mathbf{\Lambda}\mathbf{L} = \begin{bmatrix} 0 & 1 & 0 \\ -\frac{3-\gamma}{2}u^2 & (3-\gamma)u & \gamma-1 \\ \frac{\gamma-2}{2}u^3 - \frac{uc^2}{\gamma-1} & \frac{c^2}{\gamma-1} + \frac{3-2\gamma}{2}u^2 & \gamma u \end{bmatrix} \quad (4)$$

where $c = \sqrt{\gamma p / \rho}$ is the sound speed. Here, $\mathbf{\Lambda}$ is the eigen matrix of \mathbf{A} :

$$\mathbf{\Lambda} = \begin{bmatrix} u-c & & \\ & u & \\ & & u+c \end{bmatrix}, \quad (5)$$

and \mathbf{L} and \mathbf{R} are the left and right eigen vectors:

$$\mathbf{L} = \begin{bmatrix} \mathbf{l}_0 \\ \mathbf{l}_1 \\ \mathbf{l}_2 \end{bmatrix} = \begin{bmatrix} \frac{\gamma-1}{4}\frac{u^2}{c^2} + \frac{1}{2}\frac{u}{c} & -\frac{\gamma-1}{2}\frac{u}{c^2} - \frac{1}{2}\frac{1}{c} & \frac{\gamma-1}{2}\frac{1}{c^2} \\ 1 - \frac{\gamma-1}{2}\frac{u^2}{c^2} & \frac{\gamma-1}{2}\frac{u}{c^2} & -\frac{\gamma-1}{2}\frac{1}{c^2} \\ \frac{\gamma-1}{4}\frac{u^2}{c^2} - \frac{1}{2}\frac{u}{c} & -\frac{\gamma-1}{2}\frac{u}{c^2} + \frac{1}{2}\frac{1}{c} & \frac{\gamma-1}{2}\frac{1}{c^2} \end{bmatrix} \quad (6)$$

$$\mathbf{R} = [\mathbf{r}_0, \mathbf{r}_1, \mathbf{r}_2] = \begin{bmatrix} 1 & 1 & 1 \\ u-c & u & u+c \\ \frac{u^2}{2} + \frac{c^2}{\gamma-1} - uc & \frac{u^2}{2} & \frac{u^2}{2} + \frac{c^2}{\gamma-1} + uc \end{bmatrix}, \quad (7)$$

To introduce correct upwinding, the flux \vec{F} is generally splitted into two parts:

$$\vec{F} = \vec{F}^+ + \vec{F}^- \quad (8)$$

where

$$\frac{d\vec{F}^+}{d\vec{U}} \geq 0, \quad \frac{d\vec{F}^-}{d\vec{U}} < 0.$$

In this paper, the Lax-Friedrichs splitting method [2] is used:

$$\vec{F}_i^\pm = \frac{1}{2}(\vec{F}_i \pm \alpha_i \vec{U}_i). \quad (9)$$

For the Euler equations, α_i is taken as:

$$\alpha_i = \alpha = \max_i(|u_i| + c_i) \quad (10)$$

for simplicity and robustness as discussed in [2, 19].

2.2. The WENO scheme

To introduce the WENO scheme, let us consider the semi-discrete form of eq.(1) on equally spaced grid, i.e. $\Delta x = x_{i+1} - x_i$:

$$\frac{\partial \vec{U}}{\partial t} = -\frac{\partial \vec{F}}{\partial x} \approx -\frac{1}{\Delta x}(\vec{F}_{i+1/2} - \vec{F}_{i-1/2}) \quad (11)$$

where $\vec{F}_{i+1/2} = \vec{F}_{i+1/2}^+ + \vec{F}_{i+1/2}^-$ is the numerical flux at cell interface. Each component of the numerical fluxes $\vec{F}_{i+1/2}^+$ and $\vec{F}_{i+1/2}^-$, i.e. $^k \hat{f}_{i+\frac{1}{2}}^\pm$, is then reconstructed by the WENO scheme. For simplicity, k and \pm in the superscript are dropped in the following parts of this paper.

The numerical flux component $\hat{f}_{i+\frac{1}{2}}$ can be obtained by high order upwind schemes. The fifth order upwind scheme is writtend as:

$$\hat{f}_{i+\frac{1}{2}} = \frac{2}{60}f_{i+2} - \frac{13}{60}f_{i+1} + \frac{47}{60}f_i + \frac{27}{60}f_{i-1} - \frac{3}{60}f_{i-2}. \quad (12)$$

It is a convex combination of three third order upwind schemes over three sub-stencils $S_0 = (x_{i-2}, x_{i-1}, x_i)$, $S_1 = (x_{i-1}, x_i, x_{i+1})$, and $S_2 = (x_i, x_{i+1}, x_{i+2})$:

$$\hat{f}_{0,i+1/2} = \frac{1}{3}f_{i-2} - \frac{7}{6}f_{i-1} + \frac{11}{6}f_i, \quad (13)$$

$$\hat{f}_{1,i+1/2} = -\frac{1}{6}f_{i-1} + \frac{5}{6}f_i + \frac{1}{3}f_{i+1}, \quad (14)$$

$$\hat{f}_{2,i+1/2} = \frac{1}{3}f_i + \frac{5}{6}f_{i+1} - \frac{1}{6}f_{i+2}. \quad (15)$$

with linear weights $c_0 = 0.1$, $c_1 = 0.6$, and $c_2 = 0.3$ respectively. By substituting the linear weights with the non-linear WENO weights, we have the fifth order WENO scheme:

$$WENO5: \quad \hat{f}_{i+1/2} = \omega_0 \hat{f}_{0,i+1/2} + \omega_1 \hat{f}_{1,i+1/2} + \omega_2 \hat{f}_{2,i+1/2}. \quad (16)$$

The non-linear WENO weights ω_k are given by:

$$\omega_k = \frac{\alpha_k}{\sum_i \alpha_i}, \quad (17)$$

$$\alpha_k = \frac{c_k}{(\varepsilon + \beta_k)^p}, k = \{0, 1, 2\}, p = 1, 2, \dots, \quad (18)$$

where ε is a small number to avoid dividing by zero. In this paper, ε is taken to be 1.0e-6. The smoothness indicators β_i are

$$\beta_0 = \frac{13}{12}(f_{i-2} - 2f_{i-1} + f_i)^2 + \frac{1}{4}(f_{i-2} - 4f_{i-1} + 3f_i)^2, \quad (19)$$

$$\beta_1 = \frac{13}{12}(f_{i-1} - 2f_i + f_{i+1})^2 + \frac{1}{4}(f_{i-1} - f_{i+1})^2, \quad (20)$$

$$\beta_2 = \frac{13}{12}(f_i - 2f_{i+1} + f_{i+2})^2 + \frac{1}{4}(3f_i - 4f_{i+1} + f_{i+2})^2. \quad (21)$$

As shown by Henrick et al. [3], for the fifth order WENO scheme of Jiang and Shu [2], the non-linear weights do not satisfy the necessary and sufficient conditions for fifth order convergence. A mapping function was introduced to improve the accuracy of the final weights (the WENO-M scheme). In [4], Borges et al. introduced a parameter $\tau_5 = |\beta_0 - \beta_2|$ to calculate the weights as:

$$\alpha_k = c_k \left(1 + \left(\frac{\tau_5}{\beta_k + \varepsilon} \right)^q \right), k = \{0, 1, 2\}, q = 1, 2, \dots \quad (22)$$

This new scheme (the WENO-Z scheme) is less computational expensive than the WENO-M scheme. In this paper, the WENO-Z scheme is used as the base WENO scheme.

There are two ways to calculate the numerical fluxes of the Euler equations with WENO schemes, namely, the component-wise reconstruction method and the characteristic-wise reconstruction method. The former method reconstructs the numerical flux vector component-by-component while the latter method performs the reconstruction in the characteristic space. In the following two subsections (2.3 and 2.4), details of these two methods will be presented.

2.3. Component-wise reconstruction

By implementing the WENO reconstruction for the numerical flux vector \vec{F} component-by-component, the resulted numerical flux at cell interface can

be written as:

$$\vec{F}_{i+1/2}^{CP} = \begin{bmatrix} {}^0\hat{f}_{i+1/2}^{CP} \\ {}^1\hat{f}_{i+1/2}^{CP} \\ {}^2\hat{f}_{i+1/2}^{CP} \end{bmatrix} = \sum_k \omega_k^{CP} \hat{\mathbf{f}}_{k,i+1/2}^{CP} \quad (23)$$

in which

$$\omega_k^{CP} = \begin{bmatrix} {}^0\omega_k^{CP} & & \\ & {}^1\omega_k^{CP} & \\ & & {}^2\omega_k^{CP} \end{bmatrix} \quad (24)$$

and

$$\hat{\mathbf{f}}_{k,i+1/2}^{CP} = \begin{bmatrix} {}^0\hat{f}_{k,i+1/2} \\ {}^1\hat{f}_{k,i+1/2} \\ {}^2\hat{f}_{k,i+1/2} \end{bmatrix}, \quad k = 0, 1, 2. \quad (25)$$

The WENO weights in Eq.(24) are calculated according to the corresponding flux component at each stencil:

$${}^s\omega_k^{CP} = {}^s\omega_k^{CP}({}^sf_{i+k-2}, \dots, {}^sf_{i+k}), \quad k = 0, 1, 2, \quad s = 0, 1, 2, \quad (26)$$

where s is the component index and k is the stencil index. The right superscript 'CP' stands for component-wise reconstruction and the left superscript stands for the index of the component. On the right hand side of Eq.(23), the subscript k stands for variables calculated on the k -th WENO stencil corresponding to Eq.(13)-Eq.(15) for the numerical flux and Eq.(19)-Eq.(22) for the WENO weights.

It can be observed that the component-wise reconstruction method is easy to implement that only one single WENO reconstruction subroutine is needed in one's code. However, numerical oscillations may present in solutions obtained by the component-wise reconstruction method. In the following parts, the component-wise method will be referred to as the CP method.

2.4. Characteristic-wise reconstruction

Compared to the CP method, the characteristic-wise method does not produce numerical oscillations. To perform reconstruction in the characteristic space, the flux vector \vec{F} should firstly be projected onto the left eigen vector of its Jacobian (4) on cell interface $x_{i+1/2}$. The left eigen vectors on cell interface are obtained from Roe-averaged [21] primitive variables:

$$\bar{u} = \frac{\sqrt{\rho_i}u_i + \sqrt{\rho_{i+1}}u_{i+1}}{\sqrt{\rho_i} + \sqrt{\rho_{i+1}}} \quad (27)$$

$$\bar{h} = \frac{\sqrt{\rho_i}h_i + \sqrt{\rho_{i+1}}h_{i+1}}{\sqrt{\rho_i} + \sqrt{\rho_{i+1}}} \quad (28)$$

$$\bar{c} = \sqrt{(\gamma - 1)(\bar{h} - \frac{1}{2}\bar{u}^2)} \quad (29)$$

$$h = \frac{p}{(\gamma - 1)\rho} + \frac{1}{2}u^2 + \frac{p}{\rho} \quad (30)$$

The averaged left eigen vector matrix is therefore writtend as:

$$\bar{\mathbf{L}}_{i+1/2} = \begin{bmatrix} \bar{\mathbf{L}}_0 \\ \bar{\mathbf{L}}_1 \\ \bar{\mathbf{L}}_2 \end{bmatrix} = \begin{bmatrix} \frac{\gamma-1}{4}\frac{\bar{u}^2}{\bar{c}^2} + \frac{1}{2}\frac{\bar{u}}{\bar{c}} & -\frac{\gamma-1}{2}\frac{\bar{u}}{\bar{c}^2} - \frac{1}{2}\frac{1}{\bar{c}} & \frac{\gamma-1}{2}\frac{1}{\bar{c}^2} \\ 1 - \frac{\gamma-1}{2}\frac{\bar{u}^2}{\bar{c}^2} & \frac{\gamma-1}{2}\frac{\bar{u}}{\bar{c}^2} & -\frac{\gamma-1}{2}\frac{1}{\bar{c}^2} \\ \frac{\gamma-1}{4}\frac{\bar{u}^2}{\bar{c}^2} - \frac{1}{2}\frac{\bar{u}}{\bar{c}} & -\frac{\gamma-1}{2}\frac{\bar{u}}{\bar{c}^2} + \frac{1}{2}\frac{1}{\bar{c}} & \frac{\gamma-1}{2}\frac{1}{\bar{c}^2} \end{bmatrix} \quad (31)$$

The WENO reconstuction is performed component-by-component to the projected variable \hat{w} :

$$\hat{\mathbf{w}}_{k,i+1/2}^{CH} = \begin{bmatrix} {}^0\hat{w}_{k,i+1/2} \\ {}^1\hat{w}_{k,i+1/2} \\ {}^2\hat{w}_{k,i+1/2} \end{bmatrix} = \bar{\mathbf{L}}_{i+1/2} \hat{\mathbf{f}}_{k,i+1/2}^{CP}, k = 0, 1, 2 \quad (32)$$

$$\tilde{\mathbf{W}}_{i+1/2}^{CH} = \sum_{k=0}^2 \omega_k^{CH} \hat{\mathbf{w}}_{k,i+1/2}^{CH} \quad (33)$$

Different from the CP method, the WENO weights are computed according to the projected variables instead on each stencil:

$$\omega_k^{CH} = \begin{bmatrix} {}^0\omega_k^{CH} & & \\ & {}^1\omega_k^{CH} & \\ & & {}^2\omega_k^{CH} \end{bmatrix} \quad (34)$$

$${}^s\omega_k^{CH} = {}^s\omega_k^{CH}(\bar{\mathbf{L}}_s \vec{F}_{i+k-2}, \dots, \bar{\mathbf{L}}_s \vec{F}_{i+k}), \quad k = 0, 1, 2, \quad s = 0, 1, 2 \quad (35)$$

After the WENO reconstruction of the projected variables, the obtained values need to be projected back to the physics space by projecting onto the right eigen vectors on cell interface:

$$\vec{F}_{i+1/2}^{CH} = \begin{bmatrix} {}^0\hat{f}_{i+1/2}^{CH} \\ {}^1\hat{f}_{i+1/2}^{CH} \\ {}^2\hat{f}_{i+1/2}^{CH} \end{bmatrix} = \bar{\mathbf{R}}_{i+1/2} \vec{W}_{i+1/2}^{CH} \quad (36)$$

The right eigen vectors are given by:

$$\bar{\mathbf{R}}_{i+1/2} = [\bar{\mathbf{r}}_0, \bar{\mathbf{r}}_1, \bar{\mathbf{r}}_2], = \begin{bmatrix} 1 & 1 & 1 \\ \bar{u} - \bar{c} & \bar{u} & \bar{u} + \bar{c} \\ \frac{\bar{u}^2}{2} + \frac{\bar{c}^2}{\gamma-1} - \bar{u}\bar{c} & \frac{\bar{u}^2}{2} & \frac{\bar{u}^2}{2} + \frac{\bar{c}^2}{\gamma-1} + \bar{u}\bar{c} \end{bmatrix} \quad (37)$$

The whole process of the characteristic-wise WENO reconstruction can be summerized into one formula:

$$\vec{F}_{i+1/2}^{CH} = \begin{bmatrix} 0 \hat{f}_{i+1/2}^{CH} \\ 1 \hat{f}_{i+1/2}^{CH} \\ 2 \hat{f}_{i+1/2}^{CH} \end{bmatrix} = \sum_{k=0}^2 \bar{\mathbf{R}}_{i+1/2} \omega_k^{CH} \bar{\mathbf{L}}_{i+1/2} \hat{\mathbf{f}}_{k,i+1/2}^{CP}, \quad (38)$$

where the superscript 'CH' stands for characteristic-wise reconstruction. In the folloing parts, the characteristic-wise method will be refered to as the CH method.

Compared to the CP method, the CH method requires several matrix constructions and projections resulting in much more computational cost. Although the computational cost of the CH method is high, it does not produce numerical oscillations.

3. The new scheme

On one hand, in spite of its high computaional cost, the merit of the CH method is its non-oscillatory property for discontinuities. On the other hand, the advantage of the CP method is its computational efficiency regardless of the numerical oscillations it brings. Therefore, a straightforward strategy is to combine these two methods to get rid of their drawbacks and utilize their advantages. In this section, the two methods will be analyzed to show where their differences and similarities lie. A new adaptive method that combines these two method will be introduced according to our analysis.

3.1. Comparison of the two reconstruction methods

Eq.(38) can be written in a more compact form by considering:

$$\tilde{\omega}_k^{CH} = \bar{\mathbf{R}}_{i+1/2} \omega_k^{CH} \bar{\mathbf{L}}_{i+1/2}. \quad (39)$$

Subsituting Eq.(39) into Eq.(38), we have:

$$\vec{F}_{i+1/2}^{CH} = \begin{bmatrix} 0 \hat{f}_{i+1/2}^{CH} \\ 1 \hat{f}_{i+1/2}^{CH} \\ 2 \hat{f}_{i+1/2}^{CH} \end{bmatrix} = \sum_{k=0}^2 \tilde{\omega}_k^{CH} \hat{\mathbf{f}}_{k,i+1/2}^{CP} \quad (40)$$

Comparing Eq.(23) and Eq.(40), one immediately finds that the difference between the CP method and the CH method lies in their WENO weight matrices: $\tilde{\omega}_k^{CH}$ and ω_k^{CP} .

Considering smooth region, the WENO weight approximate the linear weights. Therefore, the WENO weight matrix ω_k^{CP} of the CP method becomes:

$$\omega_k^{CP} = c_k \mathbf{I}, \quad (41)$$

where \mathbf{I} is an identity matrix. For the CH method, its weight matrix $\tilde{\omega}_k^{CH}$ reads:

$$\tilde{\omega}_k^{CH} = \bar{\mathbf{R}}_{i+1/2} c_k \bar{\mathbf{L}}_{i+1/2} = c_k \bar{\mathbf{R}}_{i+1/2} \bar{\mathbf{L}}_{i+1/2}, \quad (42)$$

Note that

$$\bar{\mathbf{R}}_{i+1/2} = \bar{\mathbf{L}}_{i+1/2}^{-1}. \quad (43)$$

We have:

$$\omega_k^{CP} = c_k \mathbf{I} = \tilde{\omega}_k^{CH}. \quad (44)$$

Eq.(44) reveals that for smooth flow the numerical fluxes obtained by the two method are the same:

$$\begin{cases} \omega_k^{CP} = \bar{\mathbf{R}}_{i+1/2} \omega_k^{CH} \bar{\mathbf{L}}_{i+1/2} \\ \vec{F}_{i+1/2}^{CP} = \vec{F}_{i+1/2}^{CH} \end{cases} \quad (45)$$

For discontinuous regions, it is a different story. Let us rewrite (39) as:

$$\begin{aligned} \tilde{\omega}_k^{CH} &= \bar{\mathbf{R}}_{i+1/2} \omega_k^{CH} \bar{\mathbf{L}}_{i+1/2} \\ &= \begin{bmatrix} \bar{r}_{00} & \bar{r}_{01} & \bar{r}_{02} \\ \bar{r}_{10} & \bar{r}_{11} & \bar{r}_{12} \\ \bar{r}_{20} & \bar{r}_{21} & \bar{r}_{22} \end{bmatrix} \begin{bmatrix} {}^0\omega_k^{CH} & & \\ & {}^1\omega_k^{CH} & \\ & & {}^2\omega_k^{CH} \end{bmatrix} \begin{bmatrix} \bar{l}_{00} & \bar{l}_{01} & \bar{l}_{02} \\ \bar{l}_{10} & \bar{l}_{11} & \bar{l}_{12} \\ \bar{l}_{20} & \bar{l}_{21} & \bar{l}_{22} \end{bmatrix} \end{aligned} \quad (46)$$

Assume that numerical fluxes obtained by the two method in discontinuous situation are still the same, this means that Eq.(45) holds:

$$\omega_k^{CP} = \tilde{\omega}_k^{CH} = \bar{\mathbf{R}}_{i+1/2} \omega_k^{CH} \bar{\mathbf{L}}_{i+1/2} \quad (47)$$

Insert Eq.(46) into Eq.(47), we have:

$$\begin{bmatrix} {}^0\omega_k^{CP} & & \\ & {}^1\omega_k^{CP} & \\ & & {}^2\omega_k^{CP} \end{bmatrix} = \begin{bmatrix} \bar{r}_{00} & \bar{r}_{01} & \bar{r}_{02} \\ \bar{r}_{10} & \bar{r}_{11} & \bar{r}_{12} \\ \bar{r}_{20} & \bar{r}_{21} & \bar{r}_{22} \end{bmatrix} \begin{bmatrix} {}^0\omega_k^{CH} & & \\ & {}^1\omega_k^{CH} & \\ & & {}^2\omega_k^{CH} \end{bmatrix} \begin{bmatrix} \bar{l}_{00} & \bar{l}_{01} & \bar{l}_{02} \\ \bar{l}_{10} & \bar{l}_{11} & \bar{l}_{12} \\ \bar{l}_{20} & \bar{l}_{21} & \bar{l}_{22} \end{bmatrix} \quad (48)$$

Considering that $\bar{\mathbf{R}}_{i+1/2}\bar{\mathbf{L}}_{i+1/2} = \mathbf{I}$, Eq.(48) becomes:

$$\begin{bmatrix} \bar{l}_{00} & \bar{l}_{01} & \bar{l}_{02} \\ \bar{l}_{10} & \bar{l}_{11} & \bar{l}_{12} \\ \bar{l}_{20} & \bar{l}_{21} & \bar{l}_{22} \end{bmatrix} \begin{bmatrix} {}^0\omega_k^{CP} & & \\ & {}^1\omega_k^{CP} & \\ & & {}^2\omega_k^{CP} \end{bmatrix} = \begin{bmatrix} {}^0\omega_k^{CH} & & \\ & {}^1\omega_k^{CH} & \\ & & {}^2\omega_k^{CH} \end{bmatrix} \begin{bmatrix} \bar{l}_{00} & \bar{l}_{01} & \bar{l}_{02} \\ \bar{l}_{10} & \bar{l}_{11} & \bar{l}_{12} \\ \bar{l}_{20} & \bar{l}_{21} & \bar{l}_{22} \end{bmatrix} \quad (49)$$

After some manipulations, we obtain the following relation:

$$\begin{bmatrix} \bar{l}_{00} {}^0\omega_k^{CP} - \bar{l}_{00} {}^0\omega_k^{CH} & \bar{l}_{01} {}^1\omega_k^{CP} - \bar{l}_{01} {}^0\omega_k^{CH} & \bar{l}_{02} {}^2\omega_k^{CP} - \bar{l}_{02} {}^0\omega_k^{CH} \\ \bar{l}_{10} {}^0\omega_k^{CP} - \bar{l}_{10} {}^1\omega_k^{CH} & \bar{l}_{11} {}^1\omega_k^{CP} - \bar{l}_{11} {}^1\omega_k^{CH} & \bar{l}_{12} {}^2\omega_k^{CP} - \bar{l}_{12} {}^1\omega_k^{CH} \\ \bar{l}_{20} {}^0\omega_k^{CP} - \bar{l}_{20} {}^2\omega_k^{CH} & \bar{l}_{21} {}^1\omega_k^{CP} - \bar{l}_{21} {}^2\omega_k^{CH} & \bar{l}_{22} {}^2\omega_k^{CP} - \bar{l}_{22} {}^2\omega_k^{CH} \end{bmatrix} = \mathbf{0}, \quad (50)$$

which gives:

$${}^0\omega_k^{CP} = {}^1\omega_k^{CP} = {}^2\omega_k^{CP} = {}^0\omega_k^{CH} = {}^1\omega_k^{CH} = {}^2\omega_k^{CH}. \quad (51)$$

Now we will show that the right part of Eq.(51) does not hold for the CH method. Consider the smoothness indicators of each projected variable on the same stencil:

$$\beta_{0,\hat{w}_s} = \frac{13}{12}(\hat{w}_{s,i-2} - 2\hat{w}_{s,i-1} + \hat{w}_{s,i})^2 + \frac{1}{4}(\hat{w}_{s,i-2} - 4\hat{w}_{s,i-1} + 3\hat{w}_{s,i})^2, \quad (52)$$

$$\beta_{1,\hat{w}_s} = \frac{13}{12}(\hat{w}_{s,i-1} - 2\hat{w}_{s,i} + \hat{w}_{s,i+1})^2 + \frac{1}{4}(\hat{w}_{s,i-1} - \hat{w}_{s,i+1})^2, \quad (53)$$

$$\beta_{2,\hat{w}_s} = \frac{13}{12}(\hat{w}_{s,i} - 2\hat{w}_{s,i+1} + \hat{w}_{s,i+2})^2 + \frac{1}{4}(3\hat{w}_{s,i} - 4\hat{w}_{s,i+1} + \hat{w}_{s,i+2})^2. \quad (54)$$

Substitute $\hat{w}_{s,k}$ with:

$$\hat{w}_{s,i} = {}^0f_i\bar{l}_{s0} + {}^1f_i\bar{l}_{s1} + {}^2f_i\bar{l}_{s2}, \quad (55)$$

We have:

$$\beta_{0,\hat{w}_{s,i}} = \frac{13}{12}[\bar{l}_{s0} {}^0\Box_0 + \bar{l}_{s1} {}^1\Box_0 + \bar{l}_{s2} {}^2\Box_0]^2 + \frac{1}{4}[\bar{l}_{s0} {}^0\Delta_0 + \bar{l}_{s1} {}^1\Delta_0 + \bar{l}_{s2} {}^2\Delta_0]^2 \quad (56)$$

$$\beta_{1,\hat{w}_{s,i}} = \frac{13}{12}[\bar{l}_{s0} {}^0\Box_1 + \bar{l}_{s1} {}^1\Box_1 + \bar{l}_{s2} {}^2\Box_1]^2 + \frac{1}{4}[\bar{l}_{s0} {}^0\Diamond_0 + \bar{l}_{s1} {}^1\Diamond_0 + \bar{l}_{s2} {}^2\Diamond_0]^2 \quad (57)$$

$$\beta_{2,\hat{w}_{s,i}} = \frac{13}{12}[\bar{l}_{s0} {}^0\Box_2 + \bar{l}_{s1} {}^1\Box_2 + \bar{l}_{s2} {}^2\Box_2]^2 + \frac{1}{4}[\bar{l}_{s0} {}^0\nabla_2 + \bar{l}_{s1} {}^1\nabla_2 + \bar{l}_{s2} {}^2\nabla_2]^2, \quad (58)$$

in which:

$${}^s\Box_k = {}^sf_{i+k-2} - 2{}^sf_{i+k-1} + {}^sf_{i+k}, \quad (59)$$

$${}^s\Diamond_k = {}^sf_{i+k+1} - {}^sf_{i+k-1}, \quad (60)$$

$${}^s\Delta_k = {}^sf_{i+k-2} - 4{}^sf_{i+k-1} + 3{}^sf_{i+k}, \quad (61)$$

$${}^s\nabla_k = 3{}^sf_{i+k-2} - 4{}^sf_{i+k-1} + {}^sf_{i+k}, \quad (62)$$

$$k = 0, 1, 2; \quad s = 0, 1, 2.$$

Expanding these equations we get:

$$\begin{aligned} \beta_{0,\hat{w}_{s,i}} &= \frac{13}{12} [\bar{l}_{s0}^2 {}^0\Box_0^2 + \bar{l}_{s1}^2 {}^1\Box_0^2 + \bar{l}_{s2}^2 {}^2\Box_0^2 \\ &\quad + 2\bar{l}_{s0}\bar{l}_{s1} {}^0\Box_0^1\Box_0 + 2\bar{l}_{s1}\bar{l}_{s2} {}^1\Box_0^2\Box_0 + 2\bar{l}_{s0}\bar{l}_{s2} {}^0\Box_0^2\Box_0] \\ &\quad + \frac{1}{4} [\bar{l}_{s0}^2 {}^0\Delta_0^2 + \bar{l}_{s1}^2 {}^1\Delta_0^2 + \bar{l}_{s2}^2 {}^2\Delta_0^2 \\ &\quad + \bar{l}_{s0}\bar{l}_{s1} {}^1\Delta_0^0\Delta_0 + \bar{l}_{s0}\bar{l}_{s1} {}^1\Delta_0^0\Delta_0 + \bar{l}_{s0}\bar{l}_{s1} {}^1\Delta_0^0\Delta_0] \end{aligned} \quad (63)$$

$$\begin{aligned} \beta_{1,\hat{w}_{s,i}} &= \frac{13}{12} [\bar{l}_{s0}^2 {}^0\Box_1^2 + \bar{l}_{s1}^2 {}^1\Box_1^2 + \bar{l}_{s2}^2 {}^2\Box_1^2 \\ &\quad + 2\bar{l}_{s0}\bar{l}_{s1} {}^0\Box_1^1\Box_1 + 2\bar{l}_{s1}\bar{l}_{s2} {}^1\Box_1^2\Box_1 + 2\bar{l}_{s0}\bar{l}_{s2} {}^0\Box_1^2\Box_1] \\ &\quad + \frac{1}{4} [\bar{l}_{s0}^2 {}^0\Diamond_0^2 + \bar{l}_{s1}^2 {}^1\Diamond_0^2 + \bar{l}_{s2}^2 {}^2\Diamond_0^2 \\ &\quad + \bar{l}_{s0}\bar{l}_{s1} {}^1\Diamond_0^0\Diamond_0 + \bar{l}_{s0}\bar{l}_{s1} {}^1\Diamond_0^0\Diamond_0 + \bar{l}_{s0}\bar{l}_{s1} {}^1\Diamond_0^0\Diamond_0] \end{aligned} \quad (64)$$

$$\begin{aligned} \beta_{1,\hat{w}_{s,i}} &= \frac{13}{12} [\bar{l}_{s0}^2 {}^0\Box_2^2 + \bar{l}_{s1}^2 {}^1\Box_2^2 + \bar{l}_{s2}^2 {}^2\Box_2^2 \\ &\quad + 2\bar{l}_{s0}\bar{l}_{s1} {}^0\Box_2^1\Box_2 + 2\bar{l}_{s1}\bar{l}_{s2} {}^1\Box_2^2\Box_2 + 2\bar{l}_{s0}\bar{l}_{s2} {}^0\Box_2^2\Box_2] \\ &\quad + \frac{1}{4} [\bar{l}_{s0}^2 {}^0\nabla_2^2 + \bar{l}_{s1}^2 {}^1\nabla_2^2 + \bar{l}_{s2}^2 {}^2\nabla_2^2 \\ &\quad + \bar{l}_{s0}\bar{l}_{s1} {}^1\nabla_2^0\nabla_2 + \bar{l}_{s0}\bar{l}_{s1} {}^1\nabla_2^0\nabla_2 + \bar{l}_{s0}\bar{l}_{s1} {}^1\nabla_2^0\nabla_2] \end{aligned} \quad (65)$$

Note that

$$\begin{aligned} {}^0\beta_0 &= \frac{13}{12} {}^0\Box_0^2 + \frac{1}{4} {}^0\Delta_0^2, {}^1\beta_0 = \frac{13}{12} {}^1\Box_0^2 + \frac{1}{4} {}^1\Delta_0^2, {}^2\beta_0 = \frac{13}{12} {}^2\Box_0^2 + \frac{1}{4} {}^2\Delta_0^2 \\ {}^0\beta_1 &= \frac{13}{12} {}^0\Box_1^2 + \frac{1}{4} {}^0\Diamond_0^2, {}^1\beta_1 = \frac{13}{12} {}^1\Box_1^2 + \frac{1}{4} {}^1\Diamond_0^2, {}^2\beta_1 = \frac{13}{12} {}^2\Box_1^2 + \frac{1}{4} {}^2\Diamond_0^2 \\ {}^0\beta_2 &= \frac{13}{12} {}^0\Box_2^2 + \frac{1}{4} {}^0\nabla_2^2, {}^1\beta_2 = \frac{13}{12} {}^1\Box_2^2 + \frac{1}{4} {}^1\nabla_2^2, {}^2\beta_2 = \frac{13}{12} {}^2\Box_2^2 + \frac{1}{4} {}^2\nabla_2^2 \end{aligned} \quad (66)$$

are the smoothness indicators of each flux in physics space. Equations can be rewritten as:

$$\begin{aligned}\beta_{0,\hat{w}_{s,i}} = & \bar{l}_{s0}^2 {}^0\beta_0 + \bar{l}_{s1}^2 {}^1\beta_0 + \bar{l}_{s2}^2 {}^2\beta_0 \\ & + \frac{13}{12}[2\bar{l}_{s0}\bar{l}_{s1} {}^0\Box_0 {}^1\Box_0 + 2\bar{l}_{s1}\bar{l}_{s2} {}^1\Box_0 {}^2\Box_0 + 2\bar{l}_{s0}\bar{l}_{s2} {}^0\Box_0 {}^2\Box_0] \\ & + \frac{1}{4}[2\bar{l}_{s0}\bar{l}_{s1} {}^1\Delta_0 {}^0\Delta_0 + 2\bar{l}_{s0}\bar{l}_{s1} {}^1\Delta_0 {}^0\Delta_0 + 2\bar{l}_{s0}\bar{l}_{s1} {}^1\Delta_0 {}^0\Delta_0]\end{aligned}\quad (67)$$

$$\begin{aligned}\beta_{1,\hat{w}_{s,i}} = & \bar{l}_{s0}^2 {}^0\beta_1 + \bar{l}_{s1}^2 {}^1\beta_1 + \bar{l}_{s2}^2 {}^2\beta_1 \\ & + \frac{13}{12}[2\bar{l}_{s0}\bar{l}_{s1} {}^0\Box_1 {}^1\Box_1 + 2\bar{l}_{s1}\bar{l}_{s2} {}^1\Box_1 {}^2\Box_1 + 2\bar{l}_{s0}\bar{l}_{s2} {}^0\Box_1 {}^2\Box_1] \\ & + \frac{1}{4}[2\bar{l}_{s0}\bar{l}_{s1} {}^1\Diamond_0 {}^0\Diamond_0 + 2\bar{l}_{s0}\bar{l}_{s1} {}^1\Diamond_0 {}^0\Diamond_0 + 2\bar{l}_{s0}\bar{l}_{s1} {}^1\Diamond_0 {}^0\Diamond_0]\end{aligned}\quad (68)$$

$$\begin{aligned}\beta_{1,\hat{w}_{s,i}} = & \bar{l}_{s0}^2 {}^0\beta_2 + \bar{l}_{s1}^2 {}^1\beta_2 + \bar{l}_{s2}^2 {}^2\beta_2 \\ & + \frac{13}{12}[2\bar{l}_{s0}\bar{l}_{s1} {}^0\Box_2 {}^1\Box_2 + 2\bar{l}_{s1}\bar{l}_{s2} {}^1\Box_2 {}^2\Box_2 + 2\bar{l}_{s0}\bar{l}_{s2} {}^0\Box_2 {}^2\Box_2] \\ & + \frac{1}{4}[2\bar{l}_{s0}\bar{l}_{s1} {}^1\nabla_2 {}^0\nabla_2 + 2\bar{l}_{s0}\bar{l}_{s1} {}^1\nabla_2 {}^0\nabla_2 + 2\bar{l}_{s0}\bar{l}_{s1} {}^1\nabla_2 {}^0\nabla_2]\end{aligned}\quad (69)$$

To obtain the relation for discontinuous situation,

$${}^s\omega_k^{CH} = {}^s\omega_k^{CH} = {}^s\omega_k^{CH}$$

the ratios between each smoothness indicator of each component of \hat{w} should be equal:

$${}^0\beta_{0,\hat{w}} : {}^1\beta_{0,\hat{w}} : {}^2\beta_{0,\hat{w}} = {}^0\beta_{1,\hat{w}} : {}^1\beta_{1,\hat{w}} : {}^2\beta_{1,\hat{w}} = {}^0\beta_{2,\hat{w}} : {}^1\beta_{2,\hat{w}} : {}^2\beta_{2,\hat{w}} \quad (70)$$

It can be easily verified that, as ${}^s\beta_0$, ${}^s\beta_1$ and ${}^s\beta_2$ do not equal for discontinuous region, Eq.(70) does not hold. Therefore, for discontinuous regions, the numerical fluxes calculated by the two methods are different. As the CH method does not produce numerical oscillations near discontinuities, it is the desirable method for such circumstances.

3.2. Adaptive characteristic-wise reconstruction

According to the analysis above, the CP method and the CH method are the same in smooth region and different in discontinuous region. As the CH method does not results in numerical oscillations, it is perfered in discontinuous region. Althought the CP method produces oscillations in

some discontinuous regions, it is more computational efficient than the CH method.

A straightforward strategy to combine the advantages of these two methods is to use the CP method in smooth region and to use the CH method in discontinuous region. Therefore, a shock indicator or switch function is needed to discern these regions. To discern discontinuity accurately, we employ the switch function proposed in [22]:

$$\theta(x, z) = \frac{1}{1 + |x|^z}, \quad z \geq 1. \quad (71)$$

Fig.1 illustrates θ with different values of parameters. It transits from 1 to 0 rapidly and smoothly with increasing x . Different from tradition switches propoed for hybrid schemes, θ is free of emperimental parameters and has a high accuracy. Details about this function can be found in [22].

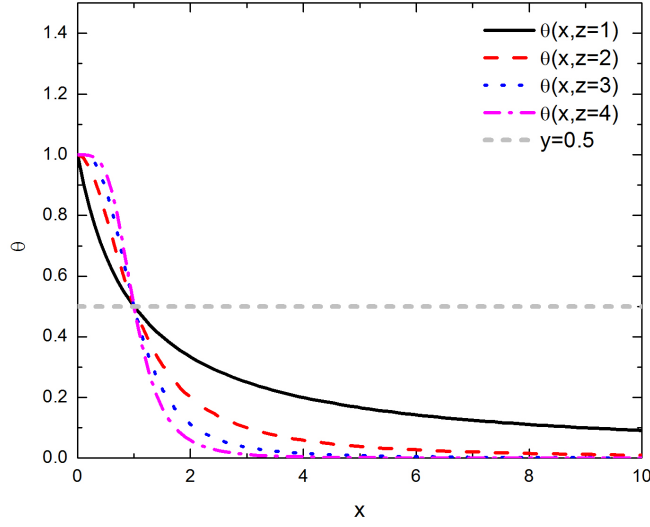


Figure 1: $\theta(x)$ with different z values

Here, we take:

$$x = \left(\sum_k \alpha_k - 1 \right)$$

and get

$$\theta = \frac{1}{1 + (\sum_k \alpha_k - 1)^z} \quad (72)$$

where α_k is the WENO non-linear weights Eq.(22). Note that for smooth region:

$$\sum_k \alpha_k \approx 1, \quad (73)$$

and for discontinuous region:

$$\sum_k \alpha_k \rightarrow \infty. \quad (74)$$

This property leads to

$$\theta = \begin{cases} 1, & \text{smooth} \\ 0, & \text{discontinuous.} \end{cases} \quad (75)$$

Taking advantage of Eq.(75), we propose the following adaptive approach:

$$\vec{F}_{i+1/2} = \begin{cases} \vec{F}_{i+1/2}^{CP}, & \theta > \theta_0 \\ \vec{F}_{i+1/2}^{CH}, & \theta \leq \theta_0 \end{cases} \quad (76)$$

where θ_0 is a threshold which can be simply taken to be:

$$\theta_0 = \theta(1, z) = 0.5. \quad (77)$$

Bearing in mind that the θ function can be interpreted as how much we believe the function being measure is smooth, it is not hard to understand the choice of θ_0 made above.

Given the addaptive method Eq.(76), an issue to be addressed is that based on which variable to calculate the non-linear weights α_k and θ . In [20], a set of WENO weights for all fluxes to be reconstructed are computed based on a set of new global smoothness indicators which are combinations of smoothness indicators of each field. Although this method reduced the number of WENO weights needed to be computed, it still calculates all the smoothness indicators. A similar method can be found in [19]. In this paper, we propose the following variable as the input of the WENO weights:

$$G^\pm = \rho + (\rho u^2 + p \pm \alpha \rho u). \quad (78)$$

Algorithm 1 The AdaWENO algorithm

- 1: Calculate G^\pm for the positive and the negative splitted fluxes \vec{F}^\pm respectively according to Eq.(78);
 - 2: **for** Each stencil $S = (i - 2, i - 1, i, i + 1, i + 2)$, $i = 1$ to n **do**
 - 3: Calculate $\beta_{k,i}^\pm$ for the positive and the negative splitted fluxes \vec{F}^\pm based on the calculated G^\pm according to Eq.(19)-(22);
 - 4: Calculate $\omega_{k,i}^{\pm,CP}$ and θ_i^\pm according to Eq.(21) and Eq.(72).
 - 5: **for** Each stencil $S = (i - 2, i - 1, i, i + 1, i + 2)$, $i = 1$ to n **do**
 - 6: **if** $\theta_i^\pm \geq 0.5$ **then**
 - 7: ${}^s\hat{f}_{i+1/2}^\pm = \sum_k \omega_{k,i}^{\pm,CP} {}^s\hat{f}_{k,i+1/2}^{\pm,CP}$, $s = 0, 1, 2$
 - 8: **else**
 - 9: ${}^s\hat{f}_{i+1/2}^\pm = {}^s\hat{f}_{i+1/2}^{\pm,CH}$, $s = 0, 1, 2$
-

Note that the \pm sign denotes G for the positive and the negative splitted flux Eq.(9) respectively. Based on G^\pm , the smoothness indicators β_k^\pm for the splitted flux is then calculated. The final WENO weights are calculated based on β_k^\pm , which a set of uniform weights for all the components of the splitted flux \vec{F}^\pm :

$$\omega_k^{\pm,CP} = {}^0\omega_k^{\pm,CP} = {}^1\omega_k^{\pm,CP} = {}^2\omega_k^{\pm,CP}, \quad k = 0, 1, 2. \quad (79)$$

In this way, we only have to calculate two sets of smoothness indicators and two sets of WENO weights. Noted that there are also two θ s should be calculated: θ^\pm .

The final adaptive characteristic-wise WENO scheme (referred as AdaWENO) algorithm is given in Algorithm 1.

4. Numerical tests

In this section, several numerical tests including one dimensional and two dimensional problems are considered to validate and evaluate the performance of the new method. Numerical results are compared between the CP method, the CH method, and AdaWENO.

The third order TVD Runge-Kutta method [23] is used for time advanc-

ing:

$$u^{(1)} = u^n + \Delta t L(u^n), \quad (80)$$

$$u^{(2)} = \frac{3}{4}u^n + \frac{1}{4}u^{(1)} + \frac{1}{4}\Delta t L(u^{(1)}), \quad (81)$$

$$u^{n+1} = \frac{1}{3}u^n + \frac{2}{3}u^{(2)} + \frac{2}{3}\Delta t L(u^{(2)}). \quad (82)$$

4.1. One dimensional cases

4.1.1. The Sod problem

The initial condition of the Sod problem is given by:

$$(\rho, u, p) = \begin{cases} (1, 0, 1) & x \leq 0 \\ (0.125, 0, 0.1) & x > 0 \end{cases} \quad (83)$$

The final solution time is $t = 0.14$. The number of uniform grids is $N = 200$. The reference result is calculated with the CH method with $N = 2000$.

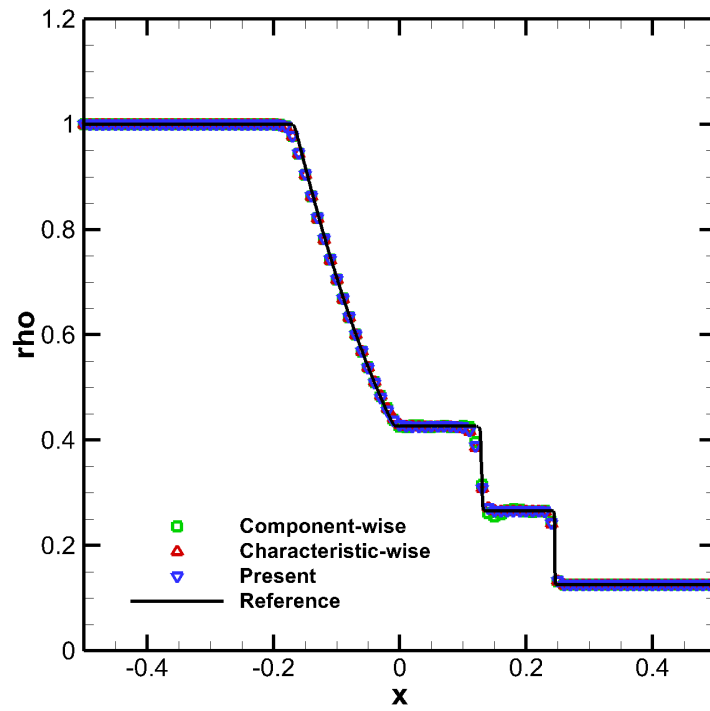


Figure 2: Density distributions of the Sod problem at $t=0.14$, $N=200$

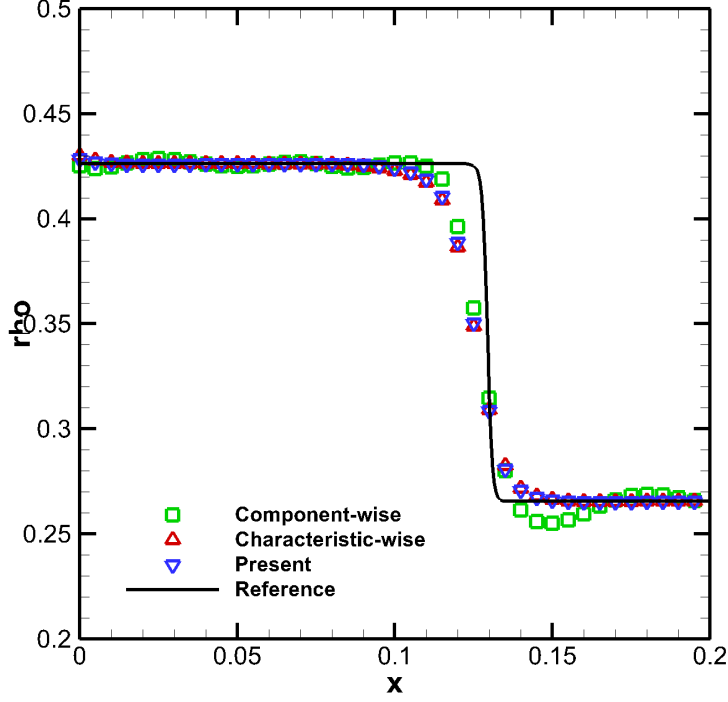


Figure 3: Zoomed density distributions near the contact discontinuity of the Sod problem

Fig.2 shows density distributions of different method at $t = 0.14$. It can be seen that the CP method produces numerical oscillations near the contact discontinuity while the other two methods do not. Zoomed distributions are shown in Fig.3. AdaWENO captures the discontinuity without obvious oscillations as with the CH method.

4.1.2. The Lax problem

The initial condition of the Lax problem is given by:

$$(\rho, u, p) = \begin{cases} (0.445, 0.698, 3.528) & x \leq 0 \\ (0.5, 0, 0.571) & x > 0 \end{cases} \quad (84)$$

Solutions are integrated to $t = 0.13$. The number of grid points is $N = 200$. The reference result is computed by the CH method with $N = 2000$.

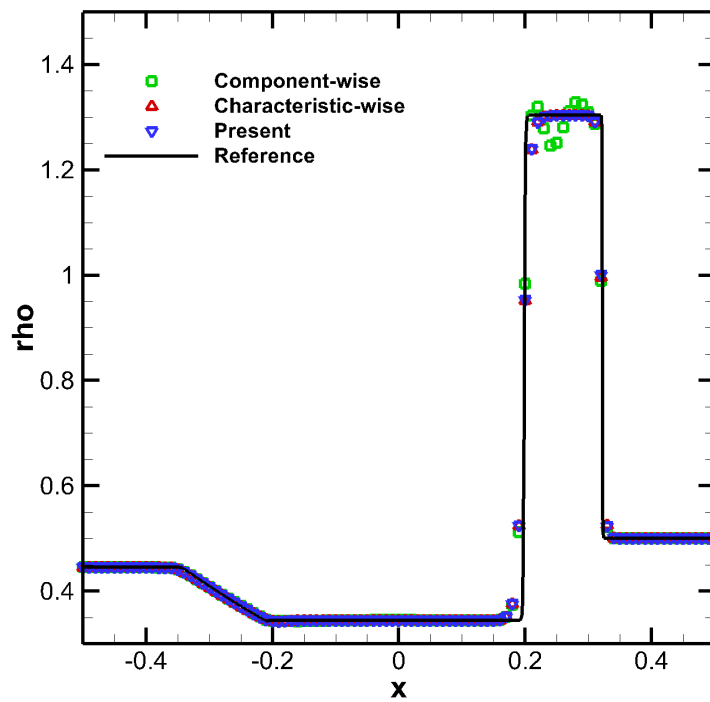


Figure 4: Density distributions of the Lax problem at $t=0.13$, $N=200$

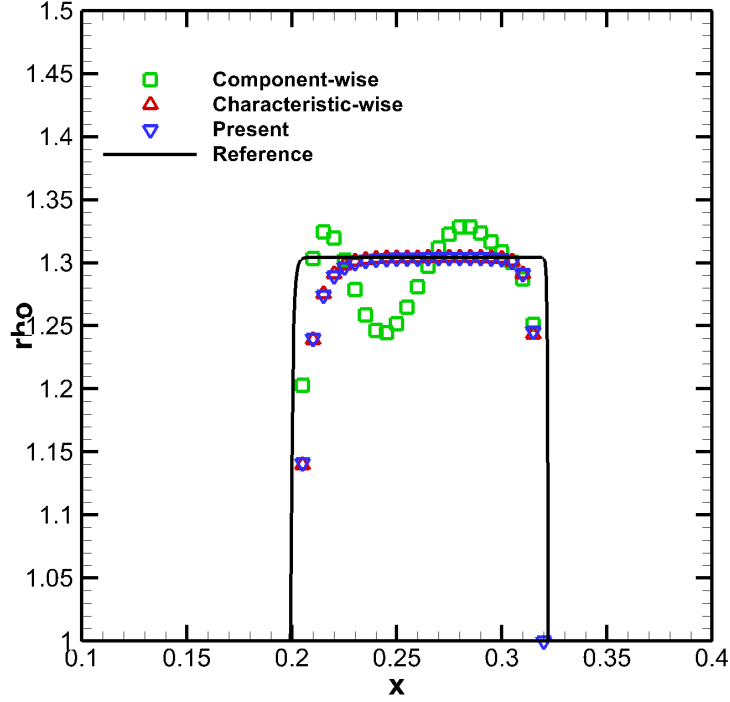


Figure 5: Zoomed density distributions near the contact discontinuity and the shock of the Lax problem

Density distributions calculated by different methods at $t = 0.13$ are shown in Fig.4. As with shown in the Sod problem, the CP method also produces numerical oscillations in vicinity of the contact discontinuity while the other two do not. Zoomed results near the contact discontinuity and the shock wave are shown in Fig.5. The new method captures the contact discontinuity and the shock wave very well. AdaWENO and the CH method show almost identical distribution.

4.1.3. Shu-Osher problem

The initial condition of the Shu-Osher problem is given by:

$$(\rho, u, p) = \begin{cases} (\frac{27}{7}, \frac{4\sqrt{35}}{9}, \frac{31}{3}) & x < -4 \\ (1 + \frac{1}{5}\sin 5x, 0, 1) & x \geq -4 \end{cases} \quad (85)$$

Solutions are integrated to $t = 1.8$. The number of grid points is $N = 200$. The reference result is computed by the CH method with $N = 2000$.

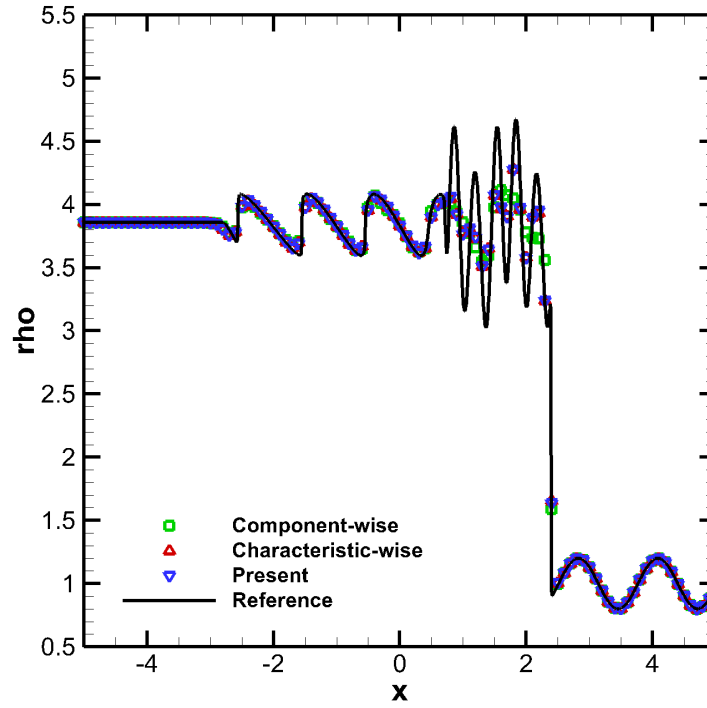


Figure 6: Density distributions of the Shu-Osher problem at $t=1.8$, $N=200$

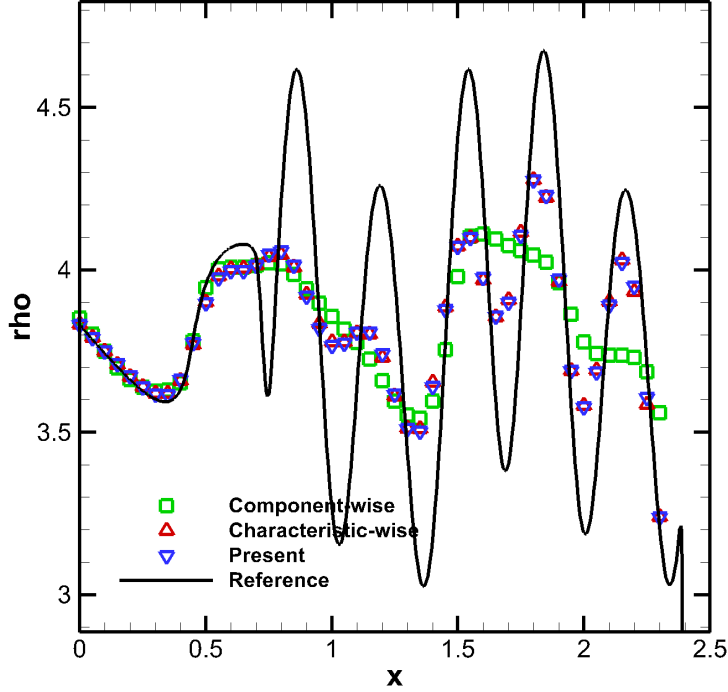


Figure 7: Zoomed density distributions near the shock of the Shu-Osher problem

Solutions of different methods are shown in Fig.6. Although short waves are not well resolved by the three method, however, near the shock wave as shown in Fig.7 AdaWENO and the CH method show better resolution of the short waves than the CP method. AdaWENO and the CH method, again, obtain almost the same result.

4.2. Two dimensional cases

4.2.1. Shock-vertex interaction

This problem describes the interaction of a stationary shock and a vertex. The computational domain is set to be $[0, 2] \times [0, 1]$. A Mach 1.1 shock is positioned at $x = 0.5$ and normal to the x-axis. Its left state is $(\rho, u, v, p) = (1, 1.1\sqrt{\gamma}, 0, 1)$ and the right states is $(\rho, u, v, p) = (1.1691, 1.1133, 0, 1.245)$. A small vortex is superposed to the flow left to the shock and centers at

$(x_x, y_c) = (0.25, 0.5)$. The initial condition to the left of the shock is given by:

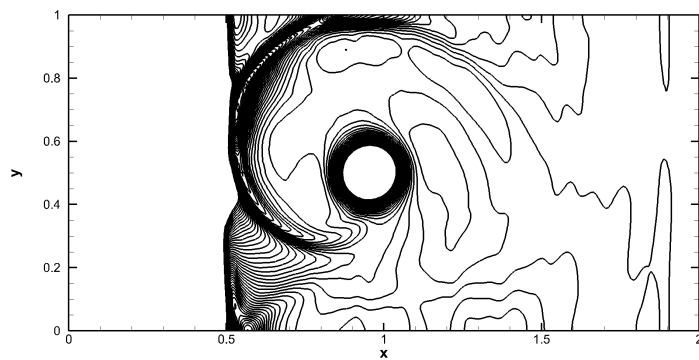
$$\rho = \left(1 - (\gamma - 1) \frac{\varepsilon^2}{4\alpha\gamma} e^{2\alpha(1-\tau^2)}\right)^{\frac{1}{\gamma-1}}, \quad (86)$$

$$u = 1.1\sqrt{\gamma} + \varepsilon\tau e^{\alpha(1-\tau^2)} \frac{(y - y_c)}{r}, \quad (87)$$

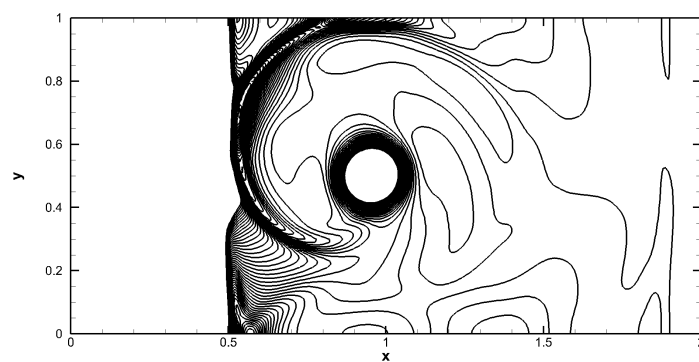
$$v = -\varepsilon\tau e^{\alpha(1-\tau^2)} \frac{(x - x_c)}{r}, \quad (88)$$

$$p = \rho^\gamma, \quad (89)$$

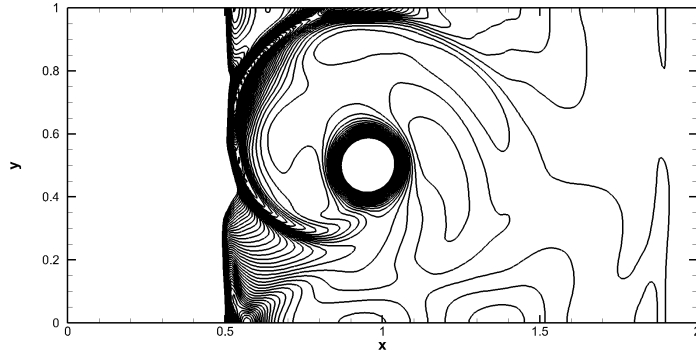
where $\tau = r/r_c$ and $r = \sqrt{(x - x_c)^2 + (y - y_c)^2}$. $\varepsilon = 0.3$ indicates the strength of the vortex, $\alpha = 0.204$ controls the decay rate of the vortex, and $r_c = 0.05$ is the critical radius for which the vortex has the maximum strength. A grid of $(N_x, N_y) = (250, 100)$ is used. The reference result is computed on a refined grid of $(N_x, N_y) = (2000, 400)$ with the CH method.



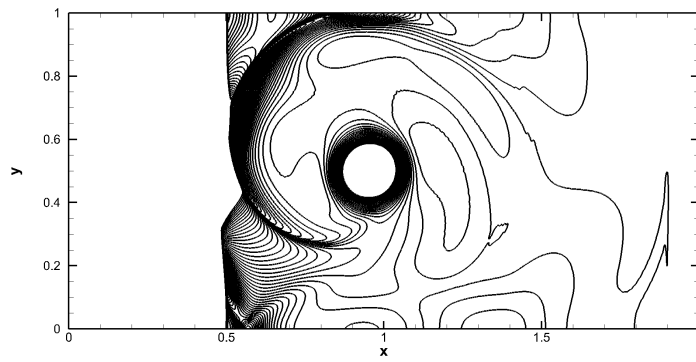
(a) Component-wise reconstruction



(b) Characteristic-wise reconstruction



(c) Present



(d) Reference

Figure 8: Pressure contours of the shock-vortex interaction problem at $t = 0.6$ with 90 equally separated levels ranging from 1.19 to 1.37.

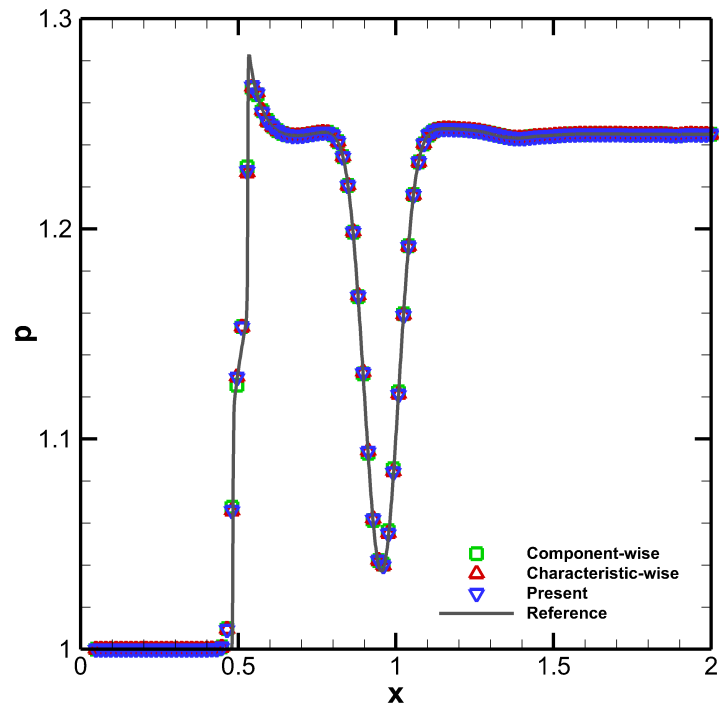
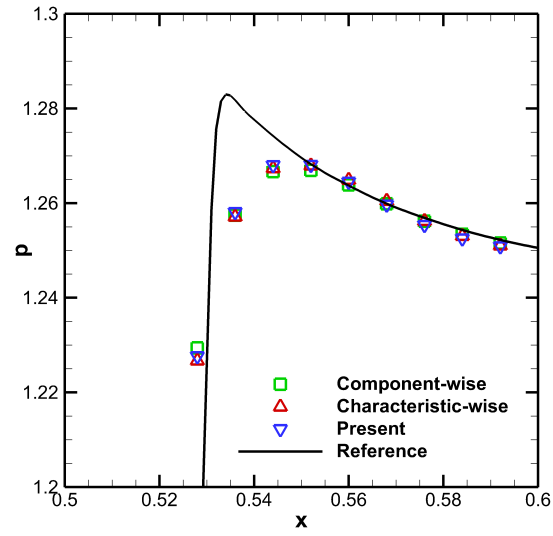
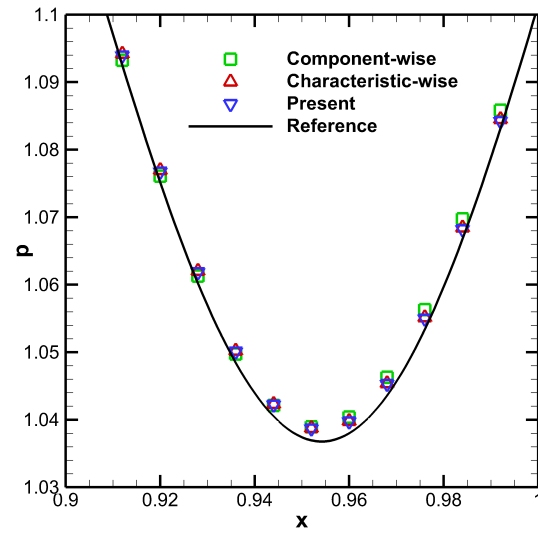


Figure 9: Pressure distributions at $y=0.5$, one of every three grid points is displayed.



(a) Near the shock



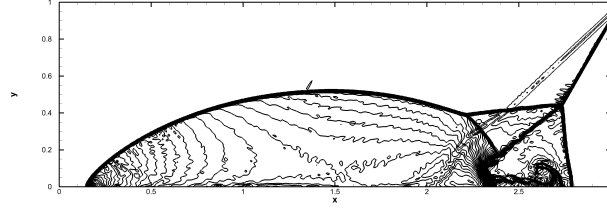
(b) Vortex center

Figure 10: Zoomed pressure distributions at $y=0.5$

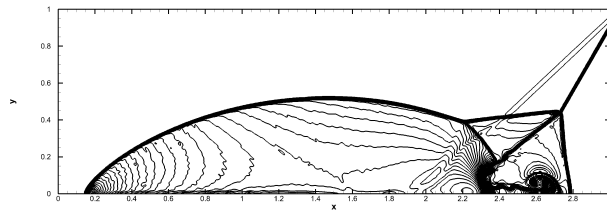
Fig.8 shows the pressure contours of different methods at $t = 0.6$. The present method obtains an almost identical result to the CH method. The CP method also gives a similar result, however, with more numerical noises. Pressure distributions of different results at $y = 0.5$ is illustrated in Fig.9. It can be seen that all methods capture the shock and the vortex well. Zoomed pressure distributions near the shock and the center of the vortex are shown in Fig.10. We find that the CH method and AdaWENO is slightly better than the CP method in these regions.

4.2.2. Double Mach reflection

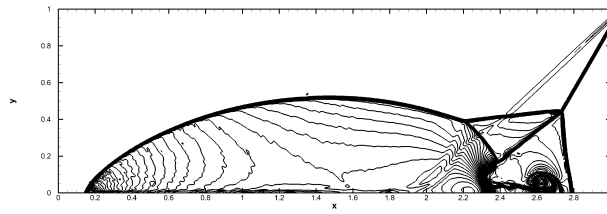
The double mach reflection test is a mimic of the planar shock reflection in the air from wedges. It is a widely used benchmark to test the ability of shock capturing and the small scale structure resolution of a certain scheme. In the present simulation, the computation domain is taken as $[0, 4] \times [0, 1]$. The lower boundary is set to be a reflecting wall starting from $x = \frac{1}{6}$. At $t = 0$, a right-moving 60° inclined Mach 10 shock is positioned at $(\frac{1}{6}, 0)$. The upper boundary is set to describe the exact motion of the Mach 10 shock. The left boundary at $x = 0$ is assigned with post-shock values. Zero gradient outflow condition is set at $x = 4$. Readers may refer to [24, 25] for detailed descriptions of the double Mach reflection problem. An uniform grid is used with $\Delta x = \Delta y = \frac{1}{240}$. The reference result is given by the CH method with $\Delta x = \Delta y = \frac{1}{480}$.



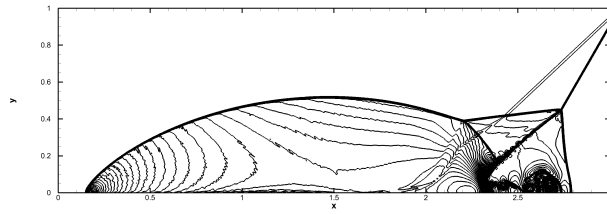
(a) Component-wise reconstruction



(b) Characteristic-wise reconstruction



(c) Present



(d) Reference

Figure 11: Density contours of the double Mach reflection problem at $t=0.2$, ranging from $\rho = 2.1379$ to 24 with 90 equally separated levels

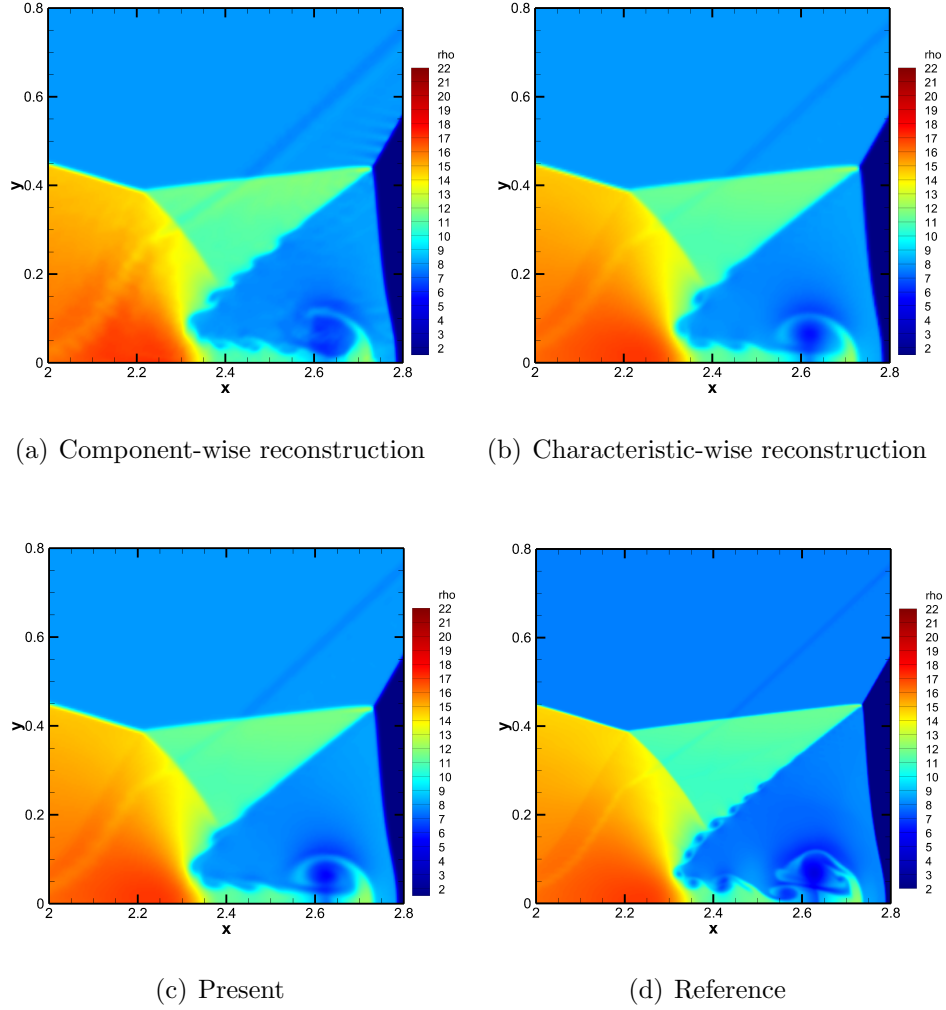


Figure 12: Density contours of the up-rolling region at $t=0.2$

Fig.11 shows density contours of different methods at $t = 0.2$. All methods capture discontinuities. The result of the CP method shows more numerical noises behind the reflected shock than the other two. Density contours of the up-rolling region of different method are shown in Fig.12. The CP method result shows obvious oscillations near the triple-wave interaction point while the CH method and the present method gives a similar and clear

Table 1: Averaged CPU times (in seconds) per time step for the double Mach reflection problem

Method	CPU time(s)/time step
CP	0.59
CH	1.09
AdaWENO	0.37

structure. Note that the two characteristic methods show few K-H instability vortices near the contact line than the CP method. It seems that the numerical oscillations produced by the CP method disturb the contact line and therefore result in more instability structures. However, the characteristic methods produce less oscillations which are not strong enough to give rise to the K-H instability structures. CPU times of different methods are given in 2, AdaWENO is about 3 times faster than the CH method and is about 40% faster than the CP method.

4.2.3. Shock/shear layer interaction

The shock wave impingement problem is designed to measure the resolution of schemes when shock waves interact with vortices [26]. A Mach 0.6 shear layer evolves and impacts on an oblique shock. The vortices produced by the shear layer instability pass, firstly, through the oblique shock and then a second shock reflected from the slip wall at the lower boundary. The computation domain is $[0, 200] \times [-20, 20]$. At $x = 0$, the inlet condition is specified as:

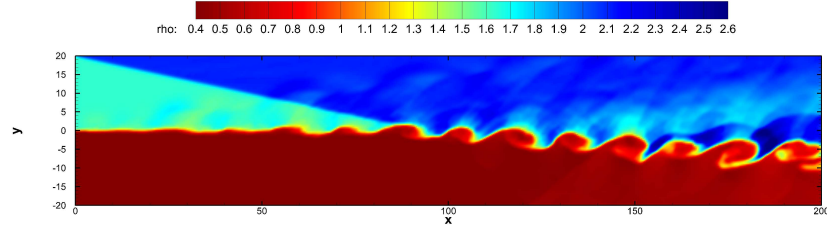
$$u = 2.5 + 0.5 \tanh(2y). \quad (90)$$

For the upper stream ($y > 0$), $\rho = 1.6374$, $p = 0.3327$ and for lower stream ($y < 0$), $\rho = 0.3626$, $p = 0.3327$. Post shock condition $(\rho, u, v, p) = (2.1101, 2.9709, -0.1367, 0.4754)$ is set at the upper boundary, and slip wall condition is applied at the lower boundary. Besides, fluctuations are added to the vertical velocity component at the inlet:

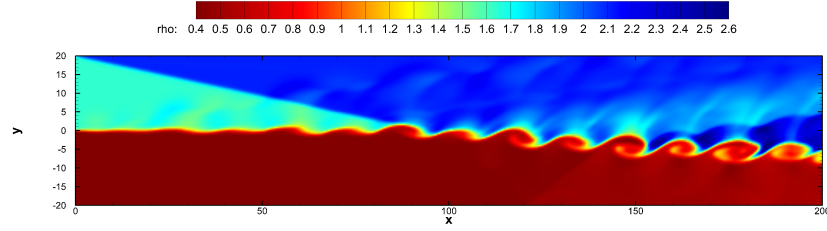
$$v' = \sum_{k=1}^2 a_k \cos(2\pi kt/T + \phi_k) \exp(-y^2/b) \quad (91)$$

$$b = 10, a_1 = a_2 = 0.05, \phi_1 = 0, \phi_2 = \pi/2 \quad (92)$$

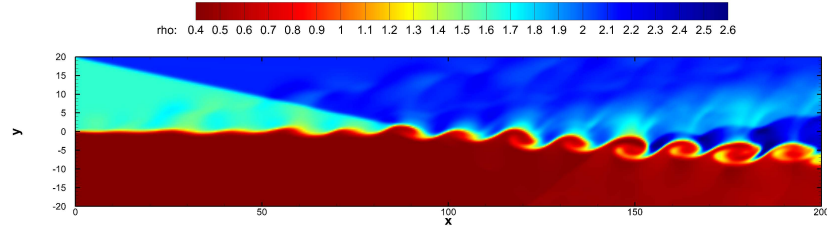
in which $T = \lambda/u_c$ is the period, $\lambda = 30$ is the wavelength, $u_c = 2.68$ is the convective velocity. The two dimensional Navier-Stokes equations are solved with the Reynolds number $Re = 500$ and the Prandtl Number $Pr = 0.72$. A equally spaced grid with grid number $(N_x, N_y) = (500, 100)$ is used. The reference result is calculated on a refined grid with $(N_x, N_y) = (2000, 400)$ by the CH method.



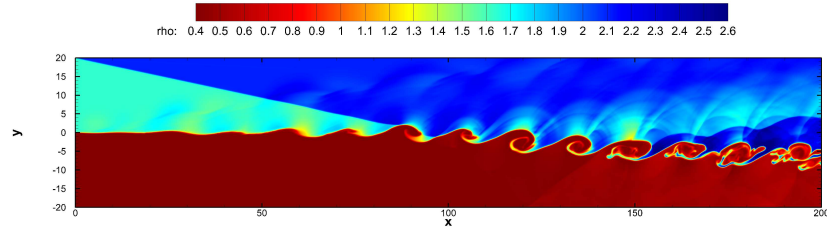
(a) Component-wise reconstruction



(b) Characteristic-wise reconstruction



(c) Present



(d) Reference

Figure 13: Density contours of the shock/shear layer interaction problem at $t=120$

Density contours are shown in Fig.13 at $t = 120$. It can be observed that the CH method and AdaWENO obtain similar results which is very comparable to the reference result, while the self-similar structure of the

Table 2: Averaged CPU times (in seconds) per time step for the shock/shear layer interaction problem

Method	CPU time(s)/time step
CP	0.13
CH	0.24
AdaWENO	0.08

downstream vortices are twisted in the CP method result. CPU times of different methods are given in 2, as having been shown in the double Mach reflection case, AdaWENO is about 3 times faster than the CH method and is about 40% faster than the CP method.

5. Conclusion

In this paper, an adaptive characteristic-wise reconstruction WENO scheme (AdaWENO) is proposed. The new method uses a high-accuracy switch function to determine the reconstruction method to be used. A new way of calculating the WENO weights is also proposed so as to reduce the overall computational cost of the WENO scheme. Numerical tests show that AdaWENO achieves high efficiency without producing any obvious numerical oscillation. AdaWENO is about 3 times faster than the CH method and about 40% faster than the CP method. With good performance and high efficiency, AdaWENO is suitable for large scale compressible flow simulations.

Acknowledgement

This research work was supported by NSFC (No.11272325 and No.11272324) and NSAF (No.U1530145) of Yiqing Shen and the Postdoctoral Science Foundation of China under Grand No.2017M610822 of Jun Peng.

References

References

- [1] X.-D. Liu, S. Osher, T. Chan, Weighted essentially non-oscillatory schemes, J. Comput. Phys. 115 (1) (1994) 200–212.

- [2] G.-S. Jiang, C.-W. Shu, Efficient implementation of weighted eno schemes, *J. Comput. Phys.* 126 (1) (1996) 202–228.
- [3] A. K. Henrick, T. A. Aslam, J. M. Powers, Mapped weighted essentially non-oscillatory schemes: achieving optimal order near critical points, *J. Comput. Phys.* 207 (2) (2005) 542–567.
- [4] R. Borges, M. Carmona, B. Costa, W. S. Don, An improved weighted essentially non-oscillatory scheme for hyperbolic conservation laws, *J. Comput. Phys.* 227 (6) (2008) 3191–3211.
- [5] M. Castro, B. Costa, W. S. Don, High order weighted essentially non-oscillatory WENO-Z schemes for hyperbolic conservation laws, *J. Comput. Phys.* 230 (5) (2011) 1766–1792.
- [6] N. K. Yamaleev, M. H. Carpenter, A systematic methodology for constructing high-order energy stable WENO schemes, *J. Comput. Phys.* 228 (11) (2009) 4248–4272.
- [7] N. K. Yamaleev, M. H. Carpenter, Third-order Energy Stable WENO scheme, *J. Comput. Phys.* 228 (8) (2009) 3025–3047.
- [8] P. Fan, Y. Shen, B. Tian, C. Yang, A new smoothness indicator for improving the weighted essentially non-oscillatory scheme, *J. Comput. Phys.* 269 (C) (2014) 329–354.
- [9] L. Fu, X. Y. Hu, N. A. Adams, A family of high-order targeted eno schemes for compressible-fluid simulations, *Journal of Computational Physics* 305 (2016) 333–359.
- [10] D. S. Balsara, C. W. Shu, Monotonicity preserving weighted essentially non-oscillatory schemes with increasingly high order of accuracy, *J. Comput. Phys.* 160 (2) (2000) 405–452.
- [11] G. A. Gerolymos, D. Sénéchal, I. Vallet, Very-high-order WENO schemes, *J. Comput. Phys.* 228 (23) (2009) 8481–8524.
- [12] M. P. Martin, E. M. Taylor, M. Wu, V. G. Weirs, A bandwidth-optimized weno scheme for the effective direct numerical simulation of compressible turbulence, *J. Comput. Phys.* 220 (1) (2006) 270–289.

- [13] Y. Shen, G. Zha, Improvement of weighted essentially non-oscillatory schemes near discontinuities, *Comput. & Fluids* 96 (C) (2014) 1–9.
- [14] Y. Shen, L. Liu, Y. Yang, Multistep weighted essentially non-oscillatory scheme, *International Journal for Numerical Methods in Fluids* 75 (4) (2014) 231–249.
- [15] J. Peng, Y. Shen, Improvement of weighted compact scheme with multi-step strategy for supersonic compressible flow, *Comput. & Fluids* 115 (0) (2015) 243–255.
- [16] A. Harten, B. Engquist, S. Osher, S. R. Chakravarthy, Uniformly high order accurate essentially non-oscillatory schemes, iii, *J. Comput. Phys.* 71 (2) (1987) 231–303.
- [17] Y.-X. Ren, M. Liu, H. Zhang, A characteristic-wise hybrid compact-weno scheme for solving hyperbolic conservation laws, *J. Comput. Phys.* 192 (2) (2003) 365–386.
- [18] S. Pirozzoli, F. Grasso, T. Gatski, Direct numerical simulation and analysis of a spatially evolving supersonic turbulent boundary layer at $m=2.25$, *Physics of fluids* 16 (3) (2004) 530–545.
- [19] Z. He, Y. Zhang, X. Li, L. Li, B. Tian, Preventing numerical oscillations in the flux-split based finite difference method for compressible flows with discontinuities, *Journal of Computational Physics* 300 (2015) 269–287.
- [20] G. Puppo, Adaptive application of characteristic projection for central schemes, in: *Hyperbolic Problems: Theory, Numerics, Applications*, Springer, 2003, pp. 819–829.
- [21] P. L. Roe, Approximate riemann solvers, parameter vectors, and difference schemes, *J. Comput. Phys.* 43 (2) (1981) 357–372.
- [22] J. Peng, Y. Shen, A novel weighting switch function for uniformly high-order hybrid shock-capturing schemes, *International Journal for Numerical Methods in Fluids* 83 (9) (2017) 681–703.
- [23] C.-W. Shu, Total-variation-diminishing time discretizations, *SIAM J. Sci. and Stat. Comput.* 9 (6) (1988) 1073–1084.

- [24] P. Woodward, P. Colella, The numerical simulation of two-dimensional fluid flow with strong shocks, *J. Comput. Phys.* 54 (1) (1984) 115–173.
- [25] F. Kemm, On the proper setup of the double mach reflection as a test case for the resolution of gas dynamics codes, *Computers & Fluids* 132 (2016) 72–75.
- [26] H. C. Yee, N. D. Sandham, M. J. Djomehri, Low-dissipative high-order shock-capturing methods using characteristic-based filters, *J. Comput. Phys.* 150 (1) (1999) 199–238.